Frequency study of functionally graded multilayer graphene platelet-reinforced polymer cylindrical panels

T. FARSADI, D. ASADI, H. KURTARAN

Adana Alparslan Türkeş Science and Technology University, Adana, Turkey,
e-mail: dasadihendoustani@atu.edu.tr

In this study, nonlinear fundamental natural frequencies of Functionally Graded (FG) multilayer Graphene Platelet-reinforced Polymer Composite (GPL-RPC) curved cylindrical panels are studied. It is considered that the Graphene Platelet (GPL) nanofillers are distributed in the matrix either uniformly or non-uniformly along the thickness direction. Four GPL distribution patterns namely, UD, FG-O, FG-X, and FG-A are considered. The effective material properties of GPL-RPC layers are obtained via the modified Halpin–Tsai micromechanics model and the rule of the mixture. A nonlinear structural model is utilized based on the virtual work principle. Green's nonlinear kinematic strain relations are used to account for the geometric nonlinearities and the First-order Shear Deformation Theory (FSDT) is adopted to generalize the formulation for the case of moderately thick cylindrical panels including transverse shear deformations. The Generalized Differential Quadrature (GDQ) method of solution is employed to solve the nonlinear governing equations of motion. The present study aims to study the effect of GPL weight fraction for the proposed distribution patterns on the nonlinear fundamental frequency of functionally graded GPL-RPC cylindrical panels with different boundary conditions.

Key words: graphene platelet-reinforced polymer, cylindrical panels, nonlinear frequency.

1. Introduction

Cylindrical and curved panels are used in many applications. Examples include missile and aircraft fuselage, aerospace structures, pipes and engine rotating components. Free and forced vibrations of cylindrical and curved panels can be investigated in terms of different material properties. In particular, the nanomaterials are valuable in industries, in which the weight to stiffness ratio of the structure plays and important role. The modern appearance of Functionally Graded Materials (FGMs) is believed to be an alternative solution for a certain class of aerospace structures [1]. Due to smoothly and continuously varying material properties from one surface to the other, FGMs are usually superior to the conventional composite materials in terms of mechanical behavior [2]. Nano-fiber reinforced materials such as carbon nanofibers, ceramic nanoparticles, carbon

nanotubes (CNTs), and graphenes attracted the attention of most researchers due to their extraordinary electrical and mechanical properties [3–4]. Graphene has been found to have its in-plane modulus up to 1.06 TPa and carbon nanotube is assessed to have a similar stiffness [5]. While CNTs can be considered as worthy candidates for the polymer matrix reinforcement to improve their mechanical characteristics, their uniform distribution in the matrix is challenging owing to their bundling generated by wall-to-wall Van der Waals interactions. Therefore, the reinforcement of polymer matrices using 2-D allotropes of carbon such as graphene has become an area of study [6].

Rafiee *et al.* [7] performed some pioneering experiments and revealed that by adding 0.1% weight fraction of GPLs, the stiffness and strength of the reinforced polymer composites are similar to the same degree achieved by adding 1% of carbon nanotubes (CNTs) and elastic modulus rises around 31%. This is because with its two dimensional attributes, distributions of graphene reinforcements in a polymer matrix are greatly improved with less agglomeration compared to the one-dimensional anisotropic CNTs. This creates a great opportunity for the development of advanced lightweight structures made of graphene based on polymer nanocomposites. Despite its influence in material design, studies on the performances of graphene-reinforced composite materials are still limited [8]. Studies can be found in the literature investigating experimentally [9], computationally [10], or analytically [11] the effect of graphene in nanocomposites.

The buckling and post-buckling analysis of FG GPL-RPC plates resting on an elastic foundation and subjected to uniaxial compression in thermal environments were studied by Shen *et al.* [12] through careful selection of material properties of graphene sheets. The governing equations are based on a higher order shear deformation plate theory with a von Karman type of kinematic nonlinearity. The presented results illustrate that the functionally graded graphene reinforcement has a substantial effect on the buckling load as well as post buckling strength of the plate. Wu *et al.* [13] investigated thermal buckling and post-buckling behaviors of GPL-RPC plates. GPL reinforcements are assumed to be uniformly distributed in each GPL-RPC layer but with the concentration varying from layer to layer. The effective Young's modulus of GPL-RPCs is predicted by a modified Halpin-Tsai micromechanics model. The nonlinear governing equations are derived based on the first-order shear deformation theory. Numerical results show that among the three GPL distribution patterns, only pattern FG-X with more GPLs distributed near the surface layers is capable of reinforcing the thermal buckling and post buckling performances of GPL-RPC plates. Reddy *et al.* [14] used the finite element method (FEM) and FSDT to study free vibration analysis of GPL-RPC plates with different boundary conditions. In this study, the effect of four different layer-wise varia-

tions of GPL distribution along the thickness as well as all possible plate edge boundary condition combinations on the natural frequencies of the plate were investigated. The effective Young's modulus for each layer and distribution type was determined using the modified Halpin–Tsai model, in which mass density and Poisson's ratio were calculated based on the rule of mixture. GUO et al. [15] investigated the vibration of laminated composite quadrilateral plates reinforced with graphene Nano-platelets using the element-free IMLS-Ritz method. They showed GPL-RPC induces a dramatically higher natural frequency in comparison with CNTRC. Additionally, the highest natural frequencies belong to the full clamped boundary condition and FG-X distribution pattern. WU et al. [16] investigated the dynamic stability of FG multilayer GPL-RPC beams in a thermal environment. Governing equations were derived based on FSDT. Accordingly, adding more GPLs and distributing them in pattern X can effectively increase the natural frequency and reduce the principal unstable region. The nonlinear vibration analysis of FG multilayer GPL-RPC beams was performed by FENG et al. [17]. In their research, a comprehensive parametric study was conducted considering the influences of distribution pattern, weight fraction, geometry, and the size of GPLs together with the total number of layers on the linear and nonlinear bending performances of the beams. Moreover, SONG et al. [18] modeled and investigated the free and forced vibration of FG multilayer GPL-RPC rectangular plates. The effects of GPL distribution pattern, weight fraction, geometry, size, and the total number of layers on the forced and free vibration of FG multilayer GPL-RPC plates were analyzed.

YANG et al. [19] investigates the buckling and post-buckling behaviors of functionally graded multilayer nanocomposite beams reinforced with a low content of GPLs resting on an elastic foundation. The results show that GPLs have a remarkable reinforcing effect on the buckling and post-buckling of nanocomposite beams. The nonlinear instability of FG GPL-RPC shells under an axial compressive load is examined by SAHMANI and AGHDAM [20]. It is observed that for both nonlocality and strain gradient size dependencies, the maximum and minimum size effects on the critical buckling loads are corresponding to FG-X and FG-O nanoshells, respectively. The terms FG-O and FG-X denote tothe GPL distribution patterns, which the FG-O model has GPLs enrich at the central layer of the plate, and FG-X has GPLs enrich at the top and bottom layers of the plate. SONG et. al. [21] investigates the biaxially compressed buckling and post-buckling behaviors of FG multilayer composite plates reinforced with a low content of GPLs that are randomly oriented and uniformly dispersed in the polymer matrix within each layer. The effects of GPL weight fraction, distribution pattern, geometry, and size as well as the total number of layers on the buckling and post-buckling behaviors of FG GPL-RPC plates are examined in detail. GHOLAMI and ANSARI [22] examine the geometrically nonlinear harmonically

excited vibration of the third-order shear deformable multilayer GPL-RPC rectangular plates with different edge conditions. The considered multilayer plate is composed of a mixture of an isotropic polymer matrix and GPLs in each layer. They found out that, to more increase the bending stiffness and strength of FG GPL-RPC plates, it is better to distribute more GPL nanofillers near the upper and bottom surfaces instead of middle layers. As a sequence, the plate with FG-X distribution pattern has the highest bending stiffness, highest natural frequency, and lowest nonlinear hardening behavior. A nonlinear buckling analysis for a clamped and simply supported FG porous GPL-RPC cylindrical shell is performed by ZHOU et al. [23]. AREFI et al. [24] analyzes the linear free vibration behavior of FG polymer composite nanoplates reinforced with graphene nanoplatelets (GNPs), resting on a Pasternak foundation. The numerical investigation shows that an FG-X pattern yields to the maximum natural frequencies, among the analyzed distributions, due to the higher bending stiffness of the composite material under this reinforcement pattern. THAI et al. [25] present the size-dependent model to study the multilayer FG GPL-RPC microplates. CONG and DUC [26] investigate the nonlinear dynamic response and vibration of FG multilayer nanocomposite plates reinforced with a low content of GPLs. The transient in-plane responses of multilayer FG GPL-RPC curved beams in a thermal environment under a concentrated moving load are investigated by BAHRANIFARD et al. [27].

Curved panels are widely used as the main components in aerospace and other modern industries. LEISSA and KADI [28] followed a shallow shell theory in order to study the effect of the curvature on the natural frequencies of curved shells. The analysis was extended to the non-linear domain by means of the Galerkin procedure and numerical integration in time. LAU and CHEUNG [29] investigated the free vibration behavior of simply supported shallow shells of rectangular planform. In [30], the effect of the thickness and the curvature upon the large-amplitude free vibrations of shallow shells was studied. Readers interested in wider reviews on vibration of curved shells and shallow shells should refer [31, 32]. Recently FARSADI et. al. [33] have conducted a study on the fundamental natural frequencies of composite curved panels.

The present work uses the Generalized Differential Quadrature (GDQ) method and the virtual work principle to study variations of the nonlinear frequency as the oscillation amplitude changes in FG multilayer GPL-RPC curved cylindrical panels at all clamped (CCCC), clamped-free-clamped-free (CFCF), and free-clamped-free-clamped (FCFC) boundary conditions. For the sake of brevity, only the fundamental frequency is discussed in the present study. Green's nonlinear strain-displacement relations are employed to formulate the mathematical model of the panel. The governing equations of motion of the GPL-RPC cylindrical panel are obtained by utilizing the virtual work principle. According to

our previous studies [34–37], spatial derivatives in the equation of motion are substituted by a weighted expansion according to the method of GDQ.

Few literature is available for using numerical methods to investigate FG GPL-RPC structures [6]. To the best of the authors' knowledge, this is the first instance of studying the nonlinear fundamental frequencies of FG GPL-RPC cylindrical panels with different curvature radius ratios and boundary conditions. To date, no research can be found in the open literature about the nonlinear analysis of large deflection of FG multilayer GPL-RPC cylindrical panels in free vibration analysis.

2. Material properties of the GPL-RPCS

Multilayer Functionally Graded (FG) Graphene Nano-Platelet (GPL) composite panel is considered. The panel includes N_L layers as shown in Fig. 1. To study the effect of the GPL dispersal on the mechanical behaviors of FG multilayer GPL-RPC cylindrical panels, four distribution patterns of GPL nanofillers across the panel thickness namely, UD, FG-O, FG-X, and FG-A are introduced. In the case of UD, the GPL content in all layers is the same. It can be observed that UD is a special case as an isotropic homogeneous panel. The FG-O contains the minimum GPL contents on both top and bottom layers of the plane and the highest GPL weight fraction in the middle-plane of the panel. The FG-X has GPLs enrich at the top and bottom layers of the panel, while Young's modulus of FG-A increases from the bottom layer to the top layer. Besides, it is seen that three patterns including UD, FG-O, and FG-X are symmetric to the mid-surface of the panel, except for FG-A. The representation of four distribution patterns of GPL nanofillers is provided in Fig. 1.
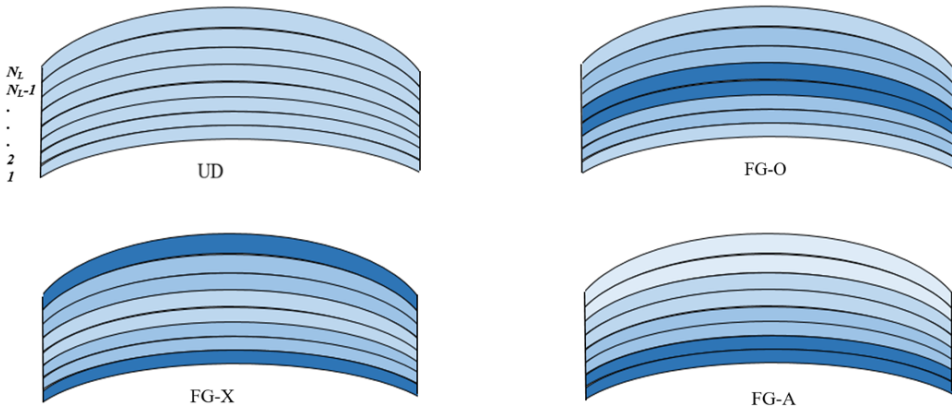

FIG. 1. Panel thickness view with four GPL distribution patterns.

The volume fractions of GPLs of the k-th layer corresponding to four considered GPL distribution patterns can be determined as:

(2.1)
$$
\begin{aligned}
\text{UD:} \quad & V_{\text{GPL}}^{(k)} = V_{\text{GPL}}^{T}, \\
\text{FG-X:} \quad & V_{\text{GPL}}^{(k)} = 2V_{\text{GPL}}^{T}|2k - N_L - 1|/N_L, \\
\text{FG-O:} \quad & V_{\text{GPL}}^{(k)} = 2V_{\text{GPL}}^{T}(1 - |2k - N_L - 1|/N_L), \\
\text{FG-A:} \quad & V_{\text{GPL}}^{(k)} = V_{\text{GPL}}^{T}(2k - 1)/N_L,
\end{aligned}
$$

in which $k = 1, 2, 3, \ldots, N_L$. V_{GPL}^{T} stands for the total volume fraction of GPLs and is calculated as:

(2.2)
$$
V_{\text{GPL}}^{T} = \frac{w_{\text{GPL}}}{w_{\text{GPL}} + (1 - w_{\text{GPL}})\left(\frac{\rho_{\text{GPL}}}{\rho_M}\right)},
$$

where the ρ_{GPL}, ρ_M, and w_{GPL} stand for the mass densities of GPL, matrix, and GPL weight fraction, respectively.

Effective Young's modulus of GPL-RPC can be theoretically determined by applying the Halpin–Tsai micromechanics approach as (see Appendix B),

(2.3)
$$
E_e^{(k)} = \frac{3}{8}\underbrace{\left(\frac{1 + \xi_L \eta_L V_{\text{GPL}}^{(k)}}{1 - \eta_L V_{\text{GPL}}^{(k)}}\right)}_{\text{longitudinal}} E_M + \frac{5}{8}\underbrace{\left(\frac{1 + \xi_T \eta_T V_{\text{GPL}}^{(k)}}{1 - \eta_T V_{\text{GPL}}^{(k)}}\right)}_{\text{transverse}} E_M,
$$

where the η_L and η_T are determined by using the following equations,

(2.4)
$$
\eta_L = \frac{E_{\text{GPL}}/E_M - 1}{E_{\text{GLP}}/E_M + \xi_L}, \quad \eta_T = \frac{E_{\text{GPL}}/E_M - 1}{E_{\text{GPL}}/E_M + \xi_T},
$$

where, E_{GPL} and E_M stand for Young's moduli of the GPLs and polymer matrix, respectively. Moreover, ξ_L and ξ_T are the internal factors, which depend on both size and geometry of GPLs nanofillers formulated as:

(2.5)
$$
\xi_L = 2\left(\frac{a_{\text{GPL}}}{h_{\text{GPL}}}\right), \quad \xi_T = 2\left(\frac{b_{\text{GPL}}}{h_{\text{GPL}}}\right),
$$

where h_{GPL}, a_{GPL} and b_{GPL} are the thickness, width and length of the GPLs, respectively. Also, the effective mass density $\rho_e^{(k)}$ and effective Poisson's ratio $\nu_e^{(k)}$ are calculated by employing the rule of the mixture as follows

(2.6)
$$
\begin{aligned}
\rho_e^{(k)} &= \rho_{\text{GPL}}V_{\text{GPL}}^{(k)} + \rho_M(1 - V_{\text{GPL}}^{(k)}), \\
\nu_e^{(k)} &= \nu_{\text{GPL}}V_{\text{GPL}}^{(k)} + \nu_M(1 - V_{\text{GPL}}^{(k)}).
\end{aligned}
$$

3. Governing equations of cylindrical panel

GPL-RPC cylindrical panel is assumed to be as the schematic illustration given in Fig. 2. According to Fig. 2, an orthogonal fixed coordinate curvilinear Cartesian system (x, φ, z) is placed at the root of the panel with a curved width a, projection of width a_p, length b, curvature radius R, and thickness h.
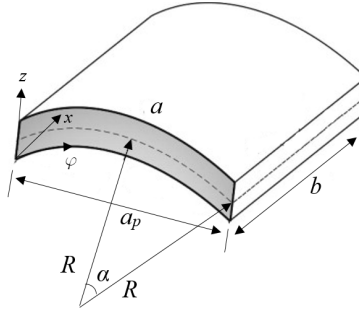

FIG. 2. Cylindrical panel geometry and the respective parameters' definitions.

The displacement field (u, v, w) of any generic point of the panel not only on the mid-surface in terms of the position coordinates (x, φ, z) and time t are given as

$$
\begin{aligned}
u(x, \varphi, z, t) &= u_0(x, \varphi, t) + z\varphi_x(x, \varphi, t), \\
v(x, \varphi, z, t) &= v_0(x, \varphi, t) + z\varphi_\phi(x, \varphi, t), \\
w(x, \varphi, z, t) &= w_0(x, \varphi, t),
\end{aligned}
$$

(3.1)

where u_0, v_0, and w_0 represent deformations of the mid-plane in x, φ and z directions, respectively, while ϕ_x, ϕ_φ are rotations about x and φ axes, respectively. On the other hand, the fully nonlinear Green strain-displacement relations for a thin elastic cylindrical panel ($\varepsilon_{zz} = 0$) are defined as the following

(3.2)
$$
\begin{Bmatrix} \varepsilon_{xx} \\ \varepsilon_{\varphi\varphi} \\ \varepsilon_{x\varphi} \\ \varepsilon_{xz} \\ \varepsilon_{\varphi z} \end{Bmatrix} = \begin{Bmatrix} \frac{\partial u}{\partial x} \\ \frac{1}{R}\left(\frac{\partial v}{\partial \phi} + w\right) \\ \frac{1}{2}\left(\frac{\partial v}{\partial x} + \frac{\partial u}{R\partial\varphi}\right) \\ \frac{1}{2}\left(\frac{\partial w}{\partial x} + \frac{\partial u}{\partial z}\right) \\ \frac{1}{2}\left(\frac{\partial v}{\partial z} + \frac{\partial w}{R\partial\varphi}\right) \end{Bmatrix} + \frac{1}{2} \begin{Bmatrix} \left(\frac{\partial u}{\partial x}\right)^2 + \left(\frac{\partial v}{\partial x}\right)^2 + \left(\frac{\partial w}{\partial x}\right)^2 \\ \frac{1}{R^2}\left[\left(\frac{\partial v}{\partial\varphi} + w\right)^2 + \left(\frac{\partial u}{\partial\varphi}\right)^2 + \left(\frac{\partial w}{\partial\varphi} - v\right)^2\right] \\ \frac{1}{R}\left[\frac{\partial w}{\partial x}\left(\frac{\partial w}{\partial\varphi} - v\right) + \frac{\partial u}{\partial\varphi}\frac{\partial u}{\partial x} + \frac{\partial v}{\partial x}\left(\frac{\partial v}{\partial\varphi} + w\right)\right] \\ \frac{\partial u}{\partial x}\frac{\partial u}{\partial z} + \frac{\partial v}{\partial x}\frac{\partial v}{\partial z} + \frac{\partial w}{\partial x}\frac{\partial w}{\partial z} \\ \frac{1}{R}\left[\frac{\partial v}{\partial z}\left(\frac{\partial v}{\partial\varphi} + w\right) + \frac{\partial u}{\partial z}\frac{\partial u}{\partial\varphi} + \frac{\partial w}{\partial z}\left(\frac{\partial w}{\partial\varphi} - v\right)\right] \end{Bmatrix}.
$$

The z/R terms are ignored in the strain-displacement equations.

Substituting the displacement field definition as given in Eq. (3.1) into the strain-displacement relations in Eq. (3.2), the following relations are determined in terms of the dependent variables u_0, v_0, w_0, ϕ_x and ϕ_ϕ

$$(3.3) \qquad \begin{Bmatrix} \varepsilon_{xx} \\ \varepsilon_{\varphi\varphi} \\ \varepsilon_{x\varphi} \\ \varepsilon_{xz} \\ \varepsilon_{\varphi z} \end{Bmatrix} = \begin{Bmatrix} \varepsilon_{xx}^{(0)} \\ \varepsilon_{\varphi\varphi}^{(0)} \\ \varepsilon_{x\varphi}^{(0)} \\ \varepsilon_{xz}^{(0)} \\ \varepsilon_{\varphi z}^{(0)} \end{Bmatrix} + z \begin{Bmatrix} \varepsilon_{xx}^{(1)} \\ \varepsilon_{\varphi\varphi}^{(1)} \\ \varepsilon_{x\phi}^{(1)} \\ \varepsilon_{xz}^{(1)} \\ \varepsilon_{\varphi z}^{(1)} \end{Bmatrix},$$

where the strains are defined as given in Eq. (3.4). Note that the subscript following each variable represents differentiation with respect to the corresponding coordinate

$$(3.4)$$
$$\begin{Bmatrix} \varepsilon_{xx}^{(0)} \\ \varepsilon_{\varphi\varphi}^{(0)} \\ \varepsilon_{x\varphi}^{(0)} \\ \varepsilon_{xz}^{(0)} \\ \varepsilon_{\varphi z}^{(0)} \end{Bmatrix} = \frac{1}{2} \begin{Bmatrix} 2u_{0,x} + u_{0,x}^2 + v_{0,x}^2 + w_{0,x}^2 \\ \frac{2}{R}(v_{0,\varphi} + w_0) + \frac{1}{R^2}[u_{0,\varphi}^2 + (v_{0,\varphi} + w_0)^2 + (w_{0,\varphi} - v_0)^2] \\ \frac{u_{0,\varphi}}{R} + v_{0,x} + \frac{1}{R}[u_{0,x}u_{0,\varphi} + v_{0,x}(v_{0,\varphi} + w_0) + w_{0,x}(w_{0,\phi} - v_0)] \\ \phi_x + w_{0,x} + u_{0,x}\phi_x + v_{0,x}\phi_\varphi \\ \frac{1}{R}[R\phi_\varphi + w_{0,\varphi} + u_{0,\varphi}\varphi_x + (v_{0,\varphi} + w_0)\phi_\varphi] \end{Bmatrix},$$

$$\begin{Bmatrix} \varepsilon_{xx}^{(1)} \\ \varepsilon_{\varphi\varphi}^{(1)} \\ \varepsilon_{x\varphi}^{(1)} \\ \varepsilon_{xz}^{(1)} \\ \varepsilon_{\varphi z}^{(1)} \end{Bmatrix} = \frac{1}{2} \begin{Bmatrix} 2\left[\phi_{x,x} + u_{0,x}\phi_{x,x} + v_{0,x}\phi_{\varphi,x}\right] \\ \frac{2}{R}\phi_{\varphi,\varphi} + \frac{2}{R^2}[u_{0,\varphi}\phi_{x,\varphi} + (v_{0,\varphi} + w_0)\phi_{\varphi,\varphi} - (w_{0,\varphi} - v_0)\phi_\varphi] \\ \frac{1}{R}[R\phi_{\varphi,x} + \phi_{x,\varphi} + u_{0,\varphi}\phi_{x,x} - w_{0,x}\phi_\varphi + \phi_{x,\varphi}u_{0,x} \\ \qquad + v_{0,x}\phi_{\varphi,\varphi} + \phi_{\varphi,x}(w_0 + v_{0,\varphi})] \\ \phi_{x,x}\phi_x + \phi_{\varphi,x}\phi_\varphi \\ \frac{1}{R}(\phi_x\phi_{x,\varphi} + \phi_\varphi\phi_{\varphi,\varphi}) \end{Bmatrix}.$$

Using the following constitutive equation for panels, one may determine the stress components in any desired lamina by the following relation

$$(3.5) \qquad \begin{Bmatrix} \sigma_{xx} \\ \sigma_{\varphi\varphi} \\ \sigma_{\varphi z} \\ \sigma_{xz} \\ \sigma_{x\varphi} \end{Bmatrix}^{(k)} = \begin{bmatrix} Q_{11}^{(k)} & Q_{12}^{(k)} & 0 & 0 & 0 \\ Q_{12}^{(k)} & Q_{22}^{(k)} & 0 & 0 & 0 \\ 0 & 0 & Q_{44}^{(k)} & 0 & 0 \\ 0 & 0 & 0 & Q_{55}^{(k)} & 0 \\ 0 & 0 & 0 & 0 & Q_{66}^{(k)} \end{bmatrix} \begin{Bmatrix} \varepsilon_{xx} \\ \varepsilon_{\varphi\varphi} \\ \varepsilon_{\varphi z} \\ \varepsilon_{xz} \\ \varepsilon_{x\varphi} \end{Bmatrix}^{(k)},$$

where the the plane stress-reduced stiffnesses at k-th layer $(Q_{ij}^{(k)})$ are defined as

$$(3.6) \qquad Q_{11}^{(k)} = Q_{22}^{(k)} = \frac{E_e^{(k)}}{1 - \nu_e^{(k)2}},$$

$$(3.7) \qquad Q_{12}^{(k)} = \frac{\nu_e^{(k)} E_e^{(k)}}{1 - \nu_e^{(k)2}},$$

$$
(3.8) \qquad Q_{44}^{(k)} = Q_{55}^{(k)} = Q_{66}^{(k)} = \frac{E_e^{(k)}}{2(1 + \nu_e^{(k)})},
$$

where E_e and ν_e being effective Young's modulus and Poisson's ratio, respectively.

In the present study, the perfect interface assumption between the composite layers is considered. But in reality, the bonding between the plies in a layered structure may not always be strong enough to preserve the structural integrity and prevent relative displacements of the adjacent layers. This can be due to manufacturing defects, or damage caused by in-service loads and environmental effects; or it can be a consequence of the presence of compliant elastic or inelastic interlayers. The zigzag theories offer a good compromise between computational simplicity and accuracy in dealing with a multilayered structures with continuous imperfect interfaces [38–41]. The present study neglects the so-called zigzag effects through the thickness displacement field caused by the differences in the shear rigidity of the layers.

To obtain the governing equations of motion for the cylindrical panel, the Hamiltonian of the structure is constructed as follows

$$
(3.9) \qquad \delta\mathcal{H} = \int_{t_1}^{t_2} \delta(T - V + W_{nc}) \, \mathrm{d}t = 0,
$$

where T and V are the kinetic and potential energies of the shell and W_{nc} is the work done by non-conservative external forces, which are neglected in the present study. The kinetic energy of the shell is defined as,

$$
(3.10) \qquad T = \frac{1}{2} \int_0^a \int_0^b \sum_{k=1}^{N_l} \int_{z_{k-1}}^{z_k} \rho^{(k)} (\dot{u}^2 + \dot{v}^2 + \dot{w}^2) R \, \mathrm{d}z \, \mathrm{d}x \, \mathrm{d}\varphi,
$$

where the over dot symbol represents differentiation with respect to the temporal coordinate and the mass density of the k-th layer is denoted by $\rho^{(k)}$. Substituting (3.1) into the kinetic energy expression given in Eq. (3.8) and performing some manipulations gives the following variational representation of the kinetic energy

$$
(3.11) \qquad \delta T = - \int_0^a \int_0^b \left[\begin{array}{l} I_0(\ddot{u}_0 \delta u_0 + \ddot{v}_0 \delta v_0 + \ddot{w}_0 \delta w_0) \\ + I_1(\ddot{\phi}_x \delta u_0 + \ddot{\phi}_\varphi \delta v_0 + \ddot{u}_0 \delta \phi_x + \ddot{v}_0 \delta \phi_\varphi) \\ + I_2(\ddot{\phi}_x \delta \phi_x + \ddot{\phi}_\varphi \delta \phi_\varphi) \end{array} \right] R \, \mathrm{d}x \, \mathrm{d}\varphi,
$$

where the following definitions are employed for the mass moments of inertia I_j $(j = 0, 1, 2)$,

$$
(3.12) \qquad \{I_0, I_1, I_2\} = \sum_{k=1}^{n} \int_{z_{k-1}}^{z_k} \{1, z, z^2\} \rho^{(k)} \, \mathrm{d}z.
$$

The next relation required to construct the Hamiltonian of the system is the elastic strain potential energy expression. The final potential expression in variational representation is defined as

$$(3.13) \quad \delta V = \int_0^a \int_0^b \sum_{k=1}^{N_l} \int_{z_{k-1}}^{z_k} \left[\begin{array}{l} \sigma_{xx}^{(k)}(\delta\varepsilon_{xx}^{(0)} + z\delta\varepsilon_{xx}^{(1)}) + \sigma_{\varphi\varphi}^{(k)}(\delta\varepsilon_{\varphi\varphi}^{(0)} + z\delta\varepsilon_{\varphi\varphi}^{(1)}) \\ + \sigma_{x\varphi}^{(k)}(\delta\varepsilon_{x\varphi}^{(0)} + z\delta\varepsilon_{x\varphi}^{(1)}) + \sigma_{xz}^{(k)}(\delta\varepsilon_{xz}^{(0)} + z\delta\varepsilon_{xz}^{(1)}) \\ + \sigma_{\varphi z}^{(k)}(\delta\varepsilon_{\varphi z}^{(0)} + z\delta\varepsilon_{\varphi z}^{(1)}) \end{array} \right]$$
$$\times R\,dz\,dx\,d\varphi.$$

Considering the shear correction factor $K_s = 5/6$ and using the definition of force and moment resultants as the following,

$$(3.14) \quad \begin{aligned} \left\{ \begin{array}{c} N_{xx}^{(i)} \\ N_{\varphi\varphi}^{(i)} \\ N_{x\varphi}^{(i)} \end{array} \right\} &= \sum_{k=1}^{N_l} \int_{z_{k-1}}^{z_k} z^i \left\{ \begin{array}{c} \sigma_{xx}^{(k)} \\ \sigma_{\varphi\varphi}^{(k)} \\ \sigma_{x\varphi}^{(k)} \end{array} \right\} dz, \quad i = 0,1, \\[2em] \left\{ \begin{array}{c} Q_{xz}^{(i)} \\ Q_{\varphi z}^{(i)} \end{array} \right\} &= \sum_{k=1}^{N_l} \int_{z_{k-1}}^{z_k} z^i K_s \left\{ \begin{array}{c} \sigma_{xz}^{(k)} \\ \sigma_{\varphi z}^{(k)} \end{array} \right\} dz, \quad i = 0,1. \end{aligned}$$

Equation (3.11) is recast to the following form,

$$(3.15) \quad \delta V = \int_0^a \int_0^b \left[\begin{array}{l} N_{xx}^{(0)}\delta\varepsilon_{xx}^{(0)} + N_{xx}^{(1)}\delta\varepsilon_{xx}^{(1)} + N_{\varphi\varphi}^{(0)}\delta\varepsilon_{\varphi\varphi}^{(0)} + N_{\varphi\varphi}^{(1)}\delta\varepsilon_{\varphi\varphi}^{(1)} \\ + N_{x\varphi}^{(0)}\delta\varepsilon_{x\varphi}^{(0)} + N_{x\varphi}^{(1)}\delta\varepsilon_{x\varphi}^{(1)} + Q_{xz}^{(0)}\delta\varepsilon_{xz}^{(0)} + Q_{xz}^{(1)}\delta\varepsilon_{xz}^{(1)} \\ + Q_{\varphi z}^{(0)}\delta\varepsilon_{\varphi z}^{(0)} + Q_{\varphi z}^{(1)}\delta\varepsilon_{\varphi z}^{(1)} \end{array} \right] R\,dx\,d\varphi.$$

According to Hamilton's principle given in Eq. (3.7), the summation of internal and inertial forces leads to the following integral representation of the governing equation of motion

$$(3.16) \quad \int_0^a \int_0^b \left[\begin{array}{l} N_{xx}^{(0)}\delta\varepsilon_{xx}^{(0)} + N_{xx}^{(1)}\delta\varepsilon_{xx}^{(1)} + N_{\varphi\varphi}^{(0)}\delta\varepsilon_{\varphi\varphi}^{(0)} + N_{\varphi\varphi}^{(1)}\delta\varepsilon_{\varphi\varphi}^{(1)} \\ + N_{x\varphi}^{(0)}\delta\varepsilon_{x\varphi}^{(0)} + N_{x\varphi}^{(1)}\delta\varepsilon_{x\varphi}^{(1)} + Q_{xz}^{(0)}\delta\varepsilon_{xz}^{(0)} + Q_{xz}^{(1)}\delta\varepsilon_{xz}^{(1)} \\ + Q_{\varphi z}^{(0)}\delta\varepsilon_{\varphi z}^{(0)} + Q_{\varphi z}^{(1)}\delta\varepsilon_{\varphi z}^{(1)} \\ + I_0(\ddot{u}_0\delta u_0 + \ddot{v}_0\delta v_0 + \ddot{w}_0\delta w_0) \\ + I_1(\ddot{\phi}_x\delta u_0 + \ddot{\phi}_\varphi\delta v_0 + \ddot{u}_0\delta\phi_x + \ddot{v}_0\delta\phi_\varphi) \\ + I_2(\ddot{\phi}_x\delta\phi_x + \ddot{\phi}_\varphi\delta\varphi_\varphi) \end{array} \right] R\,dx\,d\varphi = 0.$$

Substituting variations of the strain components from Eq. (3.4) into Eq. (3.14) gives the following explicit integral expression,

$$(3.17) \quad \int_0^a \int_0^b \begin{bmatrix} (I_0\ddot{u}_0 + I_1\ddot{\phi}_x)\delta u_0 + \mu_1\delta u_{0,x} + \mu_2\delta u_{0,\varphi} \\ + (\mu_3 + I_1\ddot{\phi}_\varphi + I_0\ddot{v}_0)\delta v_0 + \mu_4\delta v_{0,x} + \mu_5\delta v_{0,\varphi} \\ + (\mu_6 + I_0\ddot{w}_0)\delta w_0 + \mu_7\delta w_{0,x} + \mu_8\delta w_{0,\varphi} \\ + (\mu_9 + I_1\ddot{u}_0 + I_2\ddot{\phi}_x)\delta\phi_x + \mu_{10}\delta\phi_{x,x} \\ + \mu_{11}\delta\phi_{x,\varphi} + (\mu_{12} + I_2\ddot{\phi}_\varphi + I_1\ddot{v}_0)\delta\phi_\varphi \\ + \mu_{13}\delta\phi_{\varphi,x} + \mu_{14}\delta\phi_{\varphi,\varphi} \end{bmatrix} R\,\mathrm{d}x\,\mathrm{d}\varphi = 0,$$

where μ_i $(i = 1, 2, \ldots, 14)$ are defined in Appendix A.

A geometric mapping based on previous research by KURTARAN [34] is applied to facilitate numerical integrations. By implementing the proposed mapping, the curvilinear coordinate system is transformed into a bi-unit square domain. Interested readers are referred to [34] for detailed discussions on the mapping relations and sequences.

4. Solution methodology

The solution methodology includes the discretization of the curvilinear domain using the Gauss-Lobatto grid point distribution, to accommodate the application of the GDQ method to calculate the partial derivatives at grid points, and evaluate the integrals of the governing equation of motion. In what follows, a review of the GDQ is presented and then, the overall outline of the modal analysis is discussed.

4.1. Generalized differential quadrature (GDQ) method

To calculate the derivatives of the field variables in Eq. (3.17), an improved version of the GDQ method is implemented. Before the application of the GDQ method, similar to Finite Difference methods, the FG panel is discretized to grid points, representing the points, where the field variables and their derivative values are calculated. According to the GDQ method, r-th order derivative of a function $f(\xi)$ with n discrete grid points can be introduced as

$$(4.1) \qquad \left(\frac{\partial f^r(\xi)}{\partial \xi^r}\right)_{\xi_i} = \sum_{j=1}^{n} C_{ij}^{(r)} f_j,$$

where ξ_i are the discrete points in the computational domain and $C_{ij}^{(r)}$, f_j are the weighting coefficients and function values at the corresponding points, respectively. An explicit formula for the weighting coefficients based on the Lagrange polynomial for the first-order derivative, i.e. $r = 1$, is given as

$$(4.2) \qquad C_{ij}^{(1)} = \frac{\phi(\xi_i)}{(\xi_i - \xi_j)\phi(\xi_j)}, \qquad (i \neq j)$$

where

$$
(4.3) \qquad \Phi(\xi_i) = \prod_{j=1}^{n} (\xi_i - \xi_j) \quad (i \neq j).
$$

To determine the weighing coefficient values (matrix) for higher-order derivatives, the following recursive relations are proposed in the GDQ method

$$
(4.4) \qquad
\begin{aligned}
C_{ij}^{(r)} &= r \left[C_{ii}^{(r-1)} C_{ij}^{(1)} - \frac{C_{ij}^{(r-1)}}{\xi_i - \xi_j} \right] \quad (i \neq j), \\
C_{ii}^{(r)} &= - \sum_{j=1,\, i \neq j} C_{ij}^{(r)}.
\end{aligned}
$$

According to Fig. 3 partial derivates at a point (ξ_i, η_j) can be defined as follows, where n_ξ and n_η denote grid numbers in ξ and η directions, respectively,

$$
(4.5) \qquad
\begin{aligned}
\left(\frac{\partial f^r(\xi,\eta)}{\partial \xi^r} \right)_{\xi_i,\eta_j} &= \sum_{k=1}^{n_\xi} C_{kj}^{(r)} f_{kj}, \\
\left(\frac{\partial f^s(\xi,\eta)}{\partial \eta^s} \right)_{\xi_i,\eta_j} &= \sum_{m=1}^{n_\eta} C_{im}^{(s)} f_{im}, \\
\left(\frac{\partial f^{(r+s)}(\xi,\eta)}{\partial \xi^r \partial \eta^s} \right)_{\xi_i,y_j} &= \frac{\partial^r}{\partial \xi^r} \left(\frac{\partial^s f}{\partial \eta^s} \right) = \sum_{k=1}^{n_\xi} \sum_{m=1}^{n_\eta} C_{kj}^{(r)} C_{im}^{(s)} f_{km}.
\end{aligned}
$$

Note that the variables r and s denote derivative orders with respect to the variables ξ and η.
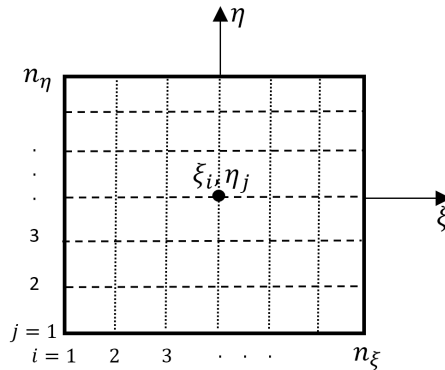

Fig. 3. Grid point distribution and the local coordinate.

One last important point is that the partial derivatives of a general function f with respect to the variables x, φ are calculated applying the GDQ method at a grid point as follows

$$(4.6) \qquad \left(\frac{\partial f}{\partial x}\right)_{ij} = \frac{1}{J_{ij}}\left[\left(\frac{\partial \varphi}{\partial \eta}\right)_{ij}\sum_{k=1}^{n_\xi}C_{kj}^{(1)}f_{kj} - \left(\frac{\partial \varphi}{\partial \xi}\right)_{ij}\sum_{m=1}^{n_\eta}C_{im}^{(1)}f_{im}\right],$$

$$(4.7) \qquad \left(\frac{\partial f}{\partial \varphi}\right)_{ij} = \frac{1}{J_{ij}}\left[\left(\frac{\partial x}{\partial \xi}\right)_{ij}\sum_{m=1}^{n_\eta}C_{im}^{(1)}f_{im} - \left(\frac{\partial x}{\partial \eta}\right)_{ij}\sum_{k=1}^{n_\xi}C_{kj}^{(1)}f_{kj}\right].$$

4.2. Free vibration analysis

The described GDQ method is applied to the governing equation in Eq. (3.15) to determine the structural matrices. The nonlinear free vibration theory applied in the present work follows the procedure given in [33, 34, 42]. For the free vibration analysis of a panel, it can be assumed that the displacements may be expressed as:

$$(4.8) \qquad w(x,\varphi,t) = Q(x,\varphi)u(t),$$

where $Q(x,\varphi)$ is the vibration pattern (the shape function) of a panel and is the harmonic time function. It can be seen in the above equation that the temporal and spatial variables in the transverse displacement function $w(x,\varphi,t)$ are assumed to be separable. $u(t)$ often takes the form of a Fourier sine series as used in [33, 34]. The numerical results from [42] indicates that there is only a very small difference between using the first term and the first two terms in the truncated Fourier sine time series. In this study, for simplicity, only one harmonic component is used. Then the imposed harmonic vibration response is assumed to be in the following form,

$$(4.9) \qquad u = \bar{u}\sin(\omega t).$$

Accordingly, the nonlinear system of equations is determined as,

$$(4.10) \qquad \mathbf{M}\ddot{u} + [\mathbf{K}_L + \mathbf{K}_{NL}^1(u) + \mathbf{K}_{NL}^2(u^2)]u = \mathbf{0},$$

where $\mathbf{K}_L$, $\mathbf{K}_{NL}^1(u)$ and $\mathbf{K}_{NL}^2(u^2)$ are respectively the linear and nonlinear stiffness matrices.

Substituting Eq. (4.9) into Eq. (4.10), the expanded view of the governing equation takes the following arrangement,

$$(4.11) \qquad -\omega^2\mathbf{M}\bar{u}\sin(\omega t) + [K\mathbf{K}_L + \mathbf{K}_{NL}^1(\bar{u}\sin(\omega t)) $$
$$+ \mathbf{K}_{NL}^2(\bar{u}^2\sin^2(\omega t))]\bar{u}\sin(\omega t) = \mathbf{0}.$$

In Eq. (4.11) nonlinear stiffness matrices $\mathbf{K}_{NL}^1(\mathbf{u})$ and $\mathbf{K}_{NL}^2(u^2)$ are time-dependent. Putting the left-hand side term equal to Γ as:

$$(4.12) \qquad \Gamma = -\omega^2 M\bar{u}\sin(\omega t) $$
$$+ [K_L + K_{NL}^1(\bar{u}\sin(\omega t)) + K_{NL}^2(\bar{u}^2\sin^2(\omega t))]\bar{u}\sin(\omega t)$$

and considering the following expression,

$$(4.13) \qquad \int\limits_{0}^{T/4} \Gamma \sin(\omega t)\, \mathrm{d}t = 0, \quad T = 2\pi\omega.$$

One finds an eigenvalue problem as established in Eq. (4.14),

$$(4.14) \qquad \left[-\omega^2 \mathbf{M} + \left(K_L + \frac{8}{3\pi} \bar{\mathbf{K}}_{NL}^1 + \frac{3}{4} \bar{\mathbf{K}}_{NL}^2 \right) \right] \bar{u} = 0,$$

where the over-bar symbol on the nonlinear stiffness matrices shows that the mentioned matrices are now in the frequency domain. Solving the presented nonlinear eigenvalue problem, the nonlinear frequency ω is determined.

In Eq. (4.14), the nonlinear stiffness matrices are a function of the normalized mode shapes. In linear eigenvalue problems, the eigenvalue and eigenvector equations generate a series of eigenvalues and their respective eigenvectors simultaneously, but from Eq. (4.14) a single eigenvalue and its corresponding eigenvector may be obtained iteratively. To calculate the nonlinear stiffness matrix in the iteration, the eigenvector cannot be used directly, it needs to be scaled according to the specified vibration amplitude at a certain location of the panel. When the fundamental nonlinear resonant frequency and mode shape are the objective, the displacement amplitude at the center of the panel may be used to scale the mode shape.

5. Numerical results

In this section, the nonlinear frequency behavior results are presented by applying the abovementioned formulation for the GPL-RPC cylindrical panels with different boundary conditions including CCCC, CFCF, and FCFC. The accuracy of the developed computer code is judged by the following verification studies.

5.1. Structural model verification

To verify the FG GPL-RPC structural model, an analytical solution [43] based on FSDT (5 DOFs), an analytical solution [24] based on refined plate theory (4 DOFs), and NURBS formulation based on the four-variable refined plate theory [8] are used. In the case of length-to-thickness ratios, $a/h = 10, 20, 50, 100$ are considered. The radius of curvature in the presented formulation is assumed to be a very large magnitude (approaching infinity). This simplifies the panel's equations to its equivalent plate configuration. Table 1 lists the effects of a/h ratio on the fundamental natural frequencies of the FG GPL-RPC with

four GPL distribution patterns including UD, FG-O, FG-X, and FG-A. It can be observed that the presented results match very well to those of referenced ones for all four patterns. Fundamental natural frequencies increase once GPLs reinforcing nanofillers are added into the polymer matrix of the plate and decrease with a rise of a/h ratio.

Table 1. The fundamental natural frequancies $\overline{\omega} = \omega h \sqrt{\rho_M / E_M}$ of the square plate.

a/h	Method	UD	FG-O	FG-X	FG-A
10	present	0.1171	0.0946	0.1350	0.1135
	[8]	0.1216	0.1023	0.1366	0.1118
	[42]	0.1216	0.1020	0.1378	1.1118
	[24]	0.1216	0.1023	0.1365	0.1118
20	present	0.0306	0.0245	0.0356	0.0296
	[8]	0.0312	0.0261	0.0355	0.0286
50	present	0.005	0.004	0.0058	0.0048
	[8]	0.005	0.0042	0.0058	0.0046
100	present	0.0013	0.001	0.0015	0.0012
	[8]	0.0013	0.001	0.0014	0.0012

To verify the geometrically nonlinear model, Fig. 4 compares the measured amplitude-dependent fundamental nonlinear frequency given by HAN and
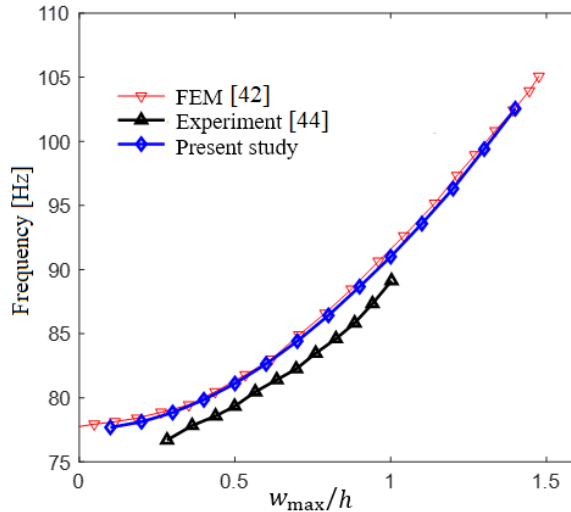

FIG. 4. The geometrically nonlinear fundamental resonant frequencies of the present study and the references [42, 44].

Petyt [42] and Benamar [44] for the isotropic rectangular plate. Dimensions of the plate are $a = 0.486$ m, $b = 0.3229$ m, and $h = 1.2$ mm. The mechanical properties of the plate are $E = 210$ GPa, $\nu = 0.3$, $\rho = 7800$ kg $\cdot$ m^{-3}. It is clear from the given results that the outcomes of the present study are in reasonable agreement with the literature.

Now that the structural model is verified in various plate configurations, it is time to take a look at the panel's formulation and find a means of verification. Table 2 shows the fundamental natural frequencies of a cylindrical panel, compared with those of Ribeiro [45] at $a_p/R = 0.4, 0.2$ with $h = 1$ mm and $a_p/R = 0.4, 0.2$ with $h = 2.5$ mm. The material properties are $E = 70$ GPa, $\nu = 0.33$, $\rho = 2778$ kg $\cdot$ m^{-3}. The small error values confirm that the presented formulations and solution strategy are correct.

Table 2. **Comparision of the fundamental natural frequency in rad/s for a cylindrical panel.**

Study	$h = 1$ mm		$h = 2.5$ mm	
	$a_p/R = 0.4$	$a_p/R = 0.2$	$a_p/R = 0.4$	$a_p/R = 0.2$
[44]	1137.61	865.359	2044.97	1662.75
Present	1136.76	864.25	2036.16	1660
Difference [%]	−0.07	−0.13	−0.43	−0.17

Further verification is performed for the free vibration analysis of the multilayered GPL reinforced cylindrical panels. Table 3 shows the first two dimensionless linear natural frequencies of the cylindrical panels with $h/R = 0.002$, $b/R = 0.1$ and simply supported, and clamped boundary conditions in comparison with those of Van Do and Lee [46]. The GPL weight fraction is set to be 1%.

Table 3. **Dimensionless natural frequencies of the cylindrical panels with simply supported and clamped boundary conditions.**

BCs.	Mode	Method	UD	FG-O	FG-X	FG-A
SSSS	1	present	13.6116	11.6927	15.2863	12.6432
		[45]	13.6144	11.6951	15.2899	12.6462
	2	present	31.4785	26.2493	35.9341	28.8675
		[45]	31.4758	26.2453	35.9313	28.8633
CCCC	1	present	24.6904	21.2045	27.7198	22.9394
		[45]	24.6929	21.2067	27.7234	22.9424
	2	present	46.6909	39.0285	53.2120	42.8710
		[45]	46.6976	39.0264	53.2100	42.8697

5.2. Results and discussions

The frequency characteristics of a cylindrical panel with three boundary conditions (CCCC, CFCF and FCFC) are considered. The nonlinear frequency behavior of the cylindrical panels with different GPL distribution patterns namely, UD, FG-O, FG-X, and FG-A and volume fractions $w_{\mathrm{GPL}}0 << 1\%$ are separately studied.

In the following provided numerical results, epoxy is chosen as the polymer matrix with Young's modulus of $E_M = 3.0$ GPa, Poisson's ratio of $\nu_M = 0.34$ and density of $\rho_M = 1200$ kg/m^3. The material properties and geometries of GPLs are chosen as Young's modulus of $E_{\mathrm{GPL}} = 1.01$ TPa, Poisson's ratio of $\nu_{\mathrm{GPL}} = 0.186$, and density of $\rho_{\mathrm{GPL}} = 1060$ kg/m^3, length of $a_{\mathrm{GPL}} = 2.5$ μm, the width of $b_{\mathrm{GPL}} = 2.5$ μm, and thickness of $h_{\mathrm{GPL}} = 1.5$ nm. The total thickness of the GPL-RPC cylindrical panel is assumed to be $a/h = 100$ and the total number of layers $N_L = 10$ are utilized in the following numerical results. Moreover, for the subsequent results, the non-dimensional linear and nonlinear frequencies are defined as $\bar{\omega} = \omega h \sqrt{\rho_M/E_M}$.

In a context where the structural performance of the curved panel is strictly related to the boundary conditions, we apply three different boundary conditions for the numerical study, namely CCCC, CFCF and FCFC where C and F denote clamped and free boundary conditions, respectively. This implies the CCCC boundary conditions,

$$(5.1) \quad \begin{aligned} x = 0, & \quad a \rightarrow u_0 = 0, \quad v_0 = 0, \quad w_0 = 0, \quad \phi_x = 0, \quad \phi_\varphi = 0, \\ y = 0, & \quad b \rightarrow u_0 = 0, \quad v_0 = 0, \quad w_0 = 0, \quad \phi_x = 0, \quad \phi_\varphi = 0, \end{aligned}$$

the CFCF,

$$(5.2) \quad \begin{aligned} x = 0, & \quad a \rightarrow u_0 = 0, \quad v_0 = 0, \quad w_0 = 0, \quad \phi_x = 0, \quad \phi_\varphi = 0, \\ y = 0, & \quad b \rightarrow -, \end{aligned}$$

and the FCFC,

$$(5.3) \quad \begin{aligned} x = 0, & \quad a \rightarrow -, \\ y = 0, & \quad b \rightarrow u_0 = 0, \quad v_0 = 0, \quad w_0 = 0, \quad \phi_x = 0, \quad \phi_\varphi = 0. \end{aligned}$$

Figures 5–7 illustrate the effect of the GPL weight fraction on the free vibration response of FG multilayer GPL-RPC cylindrical panel with CCCC, CFCF, and FCFC boundary conditions, respectively. Four distribution patterns UD, FG-O, FG-X, and FG-A with the constant GPL length to the width ratio of $a_{\mathrm{GPL}}/b_{\mathrm{GPL}} = 1$ are considered in the panel's material. The curvature radius ratios of $R/a = 2, 5, 20, \infty$ are considered in the geometrical configuration of the cylindrical panel. Figures 5–7 provide a comparison plot for the linear and
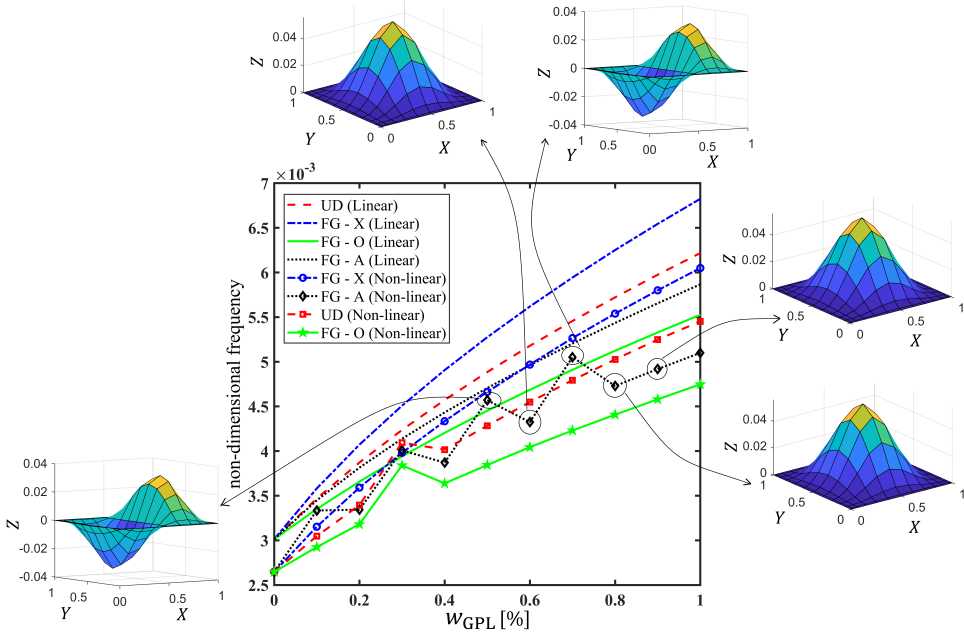
(a)
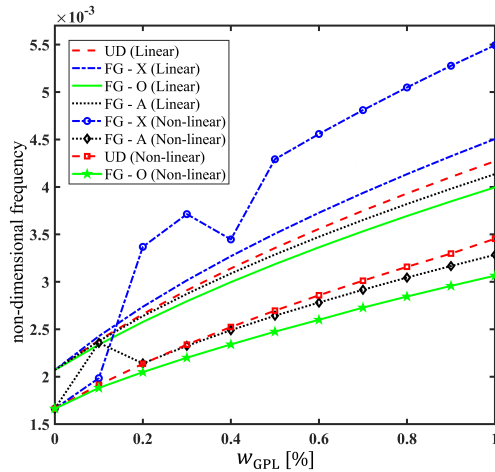
(b)

Fig. 5. Effect of GPL distribution pattern on the linear and nonlinear fundamental non-dimensional frequencies and mode shapes of FG multilayer GPL-RPC plates with CCCC boundary conditions $w_{\max}/h = 1$, $a_{\mathrm{GPL}}/b_{\mathrm{GPL}} = 1$; (a) $R/a = 2$, (b) $R/a = 5$, (c) $R/a = 20$ and (d) $R/a = \infty$.

nonlinear fundamental frequency versus the GPL weight fraction percentage ($w_{\mathrm{GPL}}0 \ll 1\%$). The nondimensional oscillation amplitude ($w_{\max}/h$) is consid-
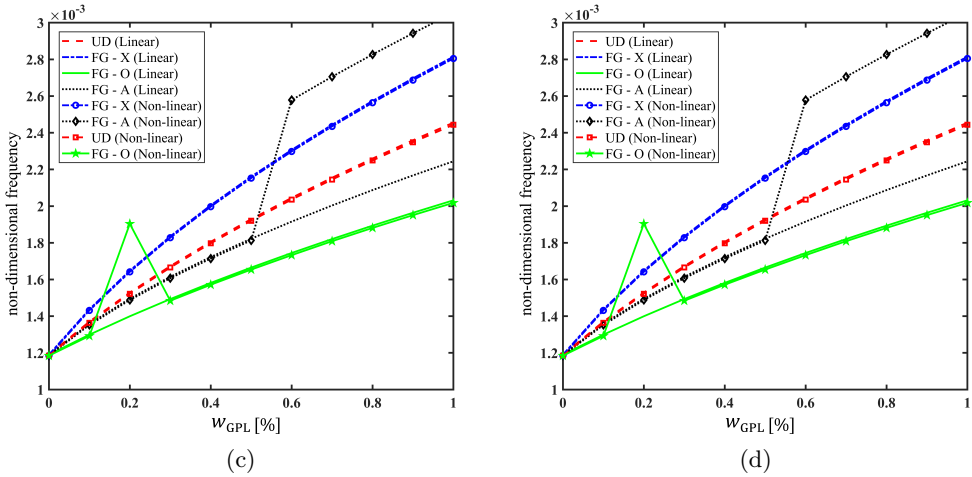
Fig. 5 [cont.]

ered to be 1, where $w_{\max}$ is the oscillation amplitude at the panel's center in the nonlinear fundamental mode of oscillation. The oscillation amplitude ($w_{\max}$) is imposed on the governing system as an initial condition. Therefore, the nonlinear frequency is calculated in each new initial conditions in nonlinear analysis. This indicates that the fundamental nonlinear frequency depends upon the amplitude of vibration, which is significantly different from the linear dynamic response.

Generally, it is observed that the linear and nonlinear fundamental frequencies of FG multilayer GPL-RPC panels continuously increase as the GPL weight fraction increases for all curvature ratios that depicts hardening behavior. It can be explained by the fact that adding more GPLs results in increasing the bending stiffness of the considered system. There are local peaks in the nonlinear frequencies in some case studies (for example, Fig. 5a, FG-A (nonlinear) branch and Fig. 5b, FG-X (nonlinear) branch). This behavior is due to the variation in the stiffness value of the GPL-RPC panels with different distribution patterns at different w_{GPL} percentages and the panel structures endeavor to the multiple stability state. These phenomena are termed as "mode switching" as mentioned in the literature. From Fig. 5a and b, it can be infered that by increasing the GPL weight fraction, the nonlinear frequencies and associated mode shapes change drastically in specific cases (for example Fig. 5a, FG-A (nonlinear) branch and Fig. 5b, FG-X (nonlinear) branch). Here the two branches are considered as case studies to show the mode switching phenomenon and its effects on sudden drops and growths in frequency diagrams. Accordingly, the switch among mode shapes are obvious in the figures.

The results indicate that with the increase of the amount of GPLs, the differences between frequencies predicted by linear and nonlinear models and consequently the hardening behavior decrease.
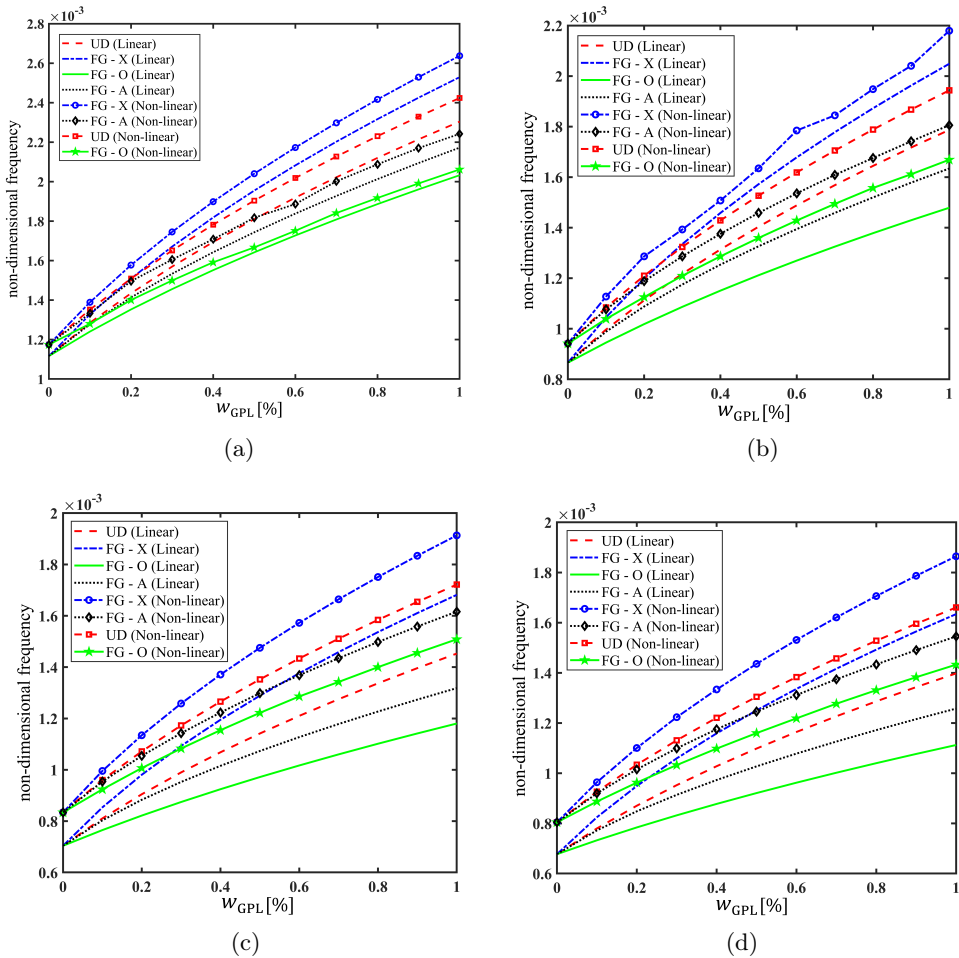
Fig. 6. Effect of GPL distribution pattern on the linear and nonlinear fundamental non-dimensional frequencies of FG multilayer GPL-RPC plates with CFCF boundary conditions $w_{max}/h = 1$, $a_{GPL}/b_{GPL} = 1$; (a) $R/a = 2$, (b) $R/a = 5$, (c) $R/a = 20$ and (d) $R/a = \infty$.

In Figures 5–7, it can be seen that the highest linear fundamental frequencies belong to the FG-X distribution pattern, which is followed by UD, FG-A, and FG-O distribution patterns for all curvature ratios and boundary conditions, respectively. It means that compared to the GPL distribution with more GPL nanofillers close to the middle plane, the FG-X distribution pattern makes better use of GPLs as the GPL nanofillers are more dispersed near the top and bottom surfaces, which are the areas undergoing higher flexural bending. Therefore, it can be deduced that to increase the total fundamental natural frequency of GPL-RPC panels, it is more effective to utilize the GPL distribution pattern by
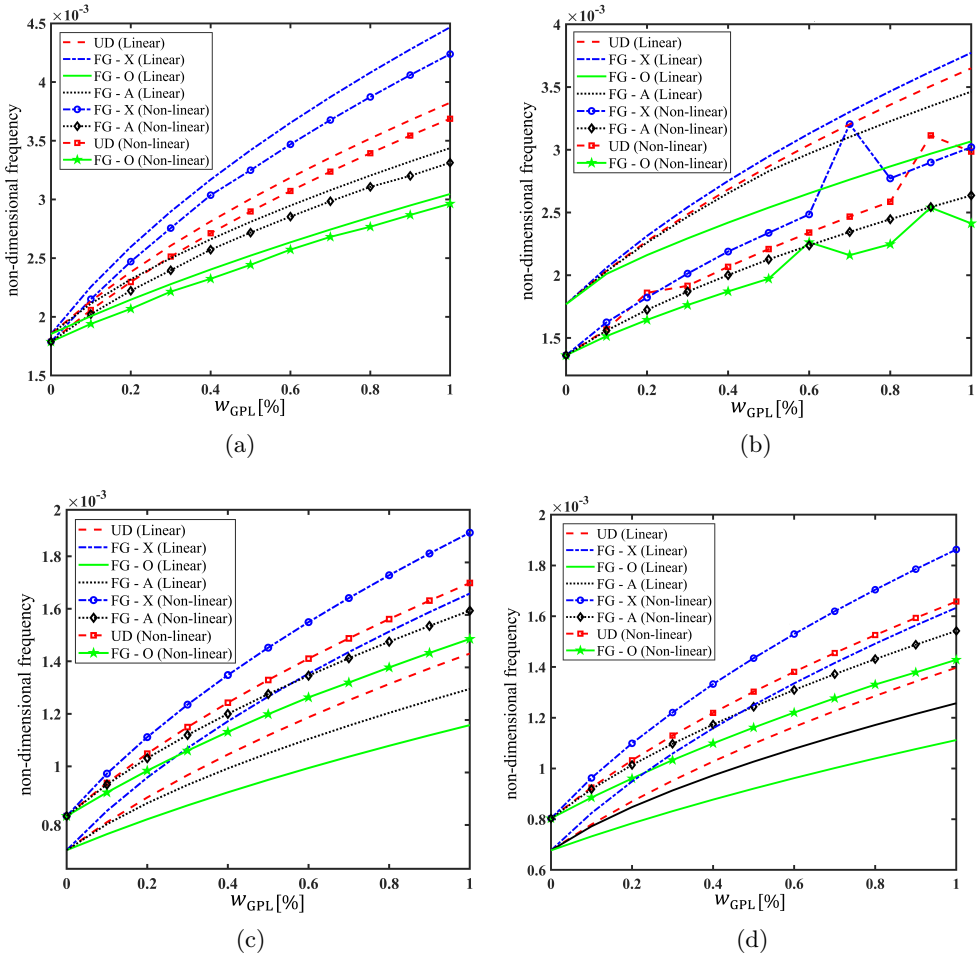
Fig. 7. Effect of GPL distribution pattern on the linear and nonlinear fundamental non-dimensional frequencies of FG multilayer GPL-RPC plates with FCFC boundary conditions $w_{\max}/h = 1$, $a_{\mathrm{GPL}}/b_{\mathrm{GPL}} = 1$; (a) $R/a = 2$, (b) $R/a = 5$, (c) $R/a = 20$ and (d) $R/a = \infty$.

dispersing more GPL nanofillers near the top and bottom surfaces of GPL-RPC panels. This is the conclusion that is extracted from the linear analysis but for the nonlinear analysis, there is an irregularity in the frequency curves for GPL distribution patterns especially in CCCC boundary conditions. The jumps in the nonlinear frequencies curve are due to the mode switching phenomena. The nonlinear frequency behavior is strongly dependent on the w_{GPL} percentages.

The curvature radius ratio also affects the fundamental frequency of linear and nonlinear panel for the different GPL weight fraction. It is observed that as the radius ratio increases, linear fundamental frequency tends to lower values
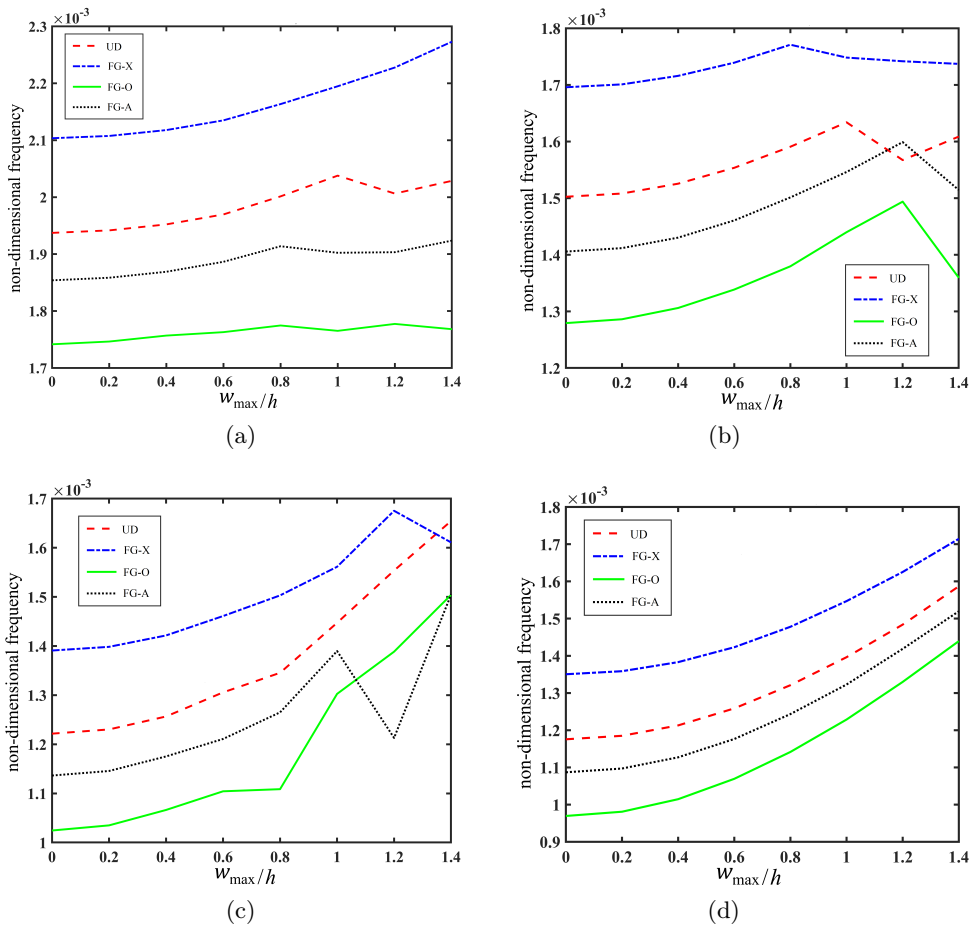
Fig. 8. Effect of GPL distribution pattern on the nonlinear fundamental non-dimensional frequencies of FG multilayer GPL-RPC panels with CFCF boundary conditions $w_{GPL} = 0.6\%$, $a_{GPL}/b_{GPL} = 1$; (a) $R/a = 2$, (b) $R/a = 5$, (c) $R/a = 20$ and (d) $R/a = \infty$.

in all four distribution patterns. So, shallow panels provide higher fundamental frequencies while stiffness in deep panels reduces significantly. Generally, the results show that with an increase in the curvature ratio, the differences between frequencies predicted by linear and nonlinear models increase. Also, in the panels with CCCC and FCFC edge conditions, the nonlinear hardening-type behavior is more considerable by increasing the curvature ratios. The differences between the estimated frequencies by the linear and nonlinear models are more pronounced in panels with $R/a = \infty$ in all boundary conditions.

The variation in GPL percentages and distribution patterns are found to affect the nonlinear frequency and degree of hardening. Figure 8 presents the

effect of the non-dimensional oscillation amplitude w_{max}/h and GPLs nanofillers distribution patterns UD, FG-O, FG-X, and FG-A on the fundamental nonlinear frequency of GPL-RPC cylindrical panels with curvature radius ratios of $R/a = 2, 5, 20, \infty$ and CFCF boundary conditions. In the numerical computations, the percentage of GPLs is kept constant by $w_{GPL} = 0.6\%$. It is showed that increasing the curvature radius ratio from $R/a = 2$ to $R/a = \infty$ (i.e. flat plate) results is significantly decreasing the nonlinear frequency due to decreasing the bending rigidity and strength of GPL-RPC cylindrical panels. There are ups and downs in the nonlinear frequencies of some case studies. This behavior is due to the change in a stiffness value of the panel at the higher amplitude of vibration and the panel structures dive to the secondary stability state.

6. Conclusions

In the present study, the effect of graphene platelet (GPL) nanofillers and their distribution patterns in the matrix on the free vibration of the cylindrical panel are explored for three types of boundary conditions. Four GPL distribution patterns namely, UD, FG-O, FG-X, and FG-A are considered. The effective material properties of GPL-RPC layers are obtained via the modified Halpin–Tsai micromechanics model and the rule of mixture. The Generalized Differential Quadrature (GDQ) method and Hamilton's principle are applied to study the variation of the fundamental frequencies of the cylindrical panels. The fundamental amplitude-dependent nonlinear frequency behavior of the GPL-RPC panel is studied and compared. According to the results, different boundary conditions, GPL distribution pattern, GPL weight fraction, and radius ratios significantly affect the curved panel's natural and nonlinear fundamental frequencies and mode shapes as well as affecting the maximum achievable frequency.

- GPL volume fraction plays an important role on significantly improving the linear vibration performance of the curved panels.
- Generally, the FG-X model with high GPL concentration in the layers close to the top and bottom shows the best performance in increasing the fundamental natural frequencies both linearly and nonlinearly.
- The fundamental natural frequency decreases as the radius curvature ratio increases from 2 to ∞ for almost all GPL models and boundary conditions.
- In the panels with CCCC and FCFC edge conditions, the nonlinear hardening-type behavior is more considerable by increasing the curvature ratios.
- The obtained results reveal that panels with moderate curvature ratios are more prone to experience mode switchings.
- The nonlinear results in CFCF configuration show that, generally for radius ratios from 2 to ∞, increase of an oscillation amplitude leads to an

increase of nonlinear stiffness (hardening) and thus higher nonlinear frequency ratios are achieved. This is not valid when the mode switching phenomenon happens in the panels with curvature ratios of 5 and 20.

Appendix A

Definitions of the μ_i, $i = 1, 2, \ldots, 14$ parameters used in Eq. (3.15) are presented in terms of the displacement variables as well as force/moment resultants

$$\mu_1 = N_{xx}^{(0)}(1 + u_{0,x}) + N_{xx}^{(1)}\phi_{x,x} + \frac{1}{2R}(N_{x\varphi}^{(0)}u_{0,\varphi} + N_{x\varphi}^{(1)}\phi_{x,\varphi} + RQ_{xz}^{(0)}\phi_x),$$

$$\mu_2 = \frac{1}{2R^2}[2N_{\varphi\varphi}^{(0)}u_{0,\varphi} + 2N_{\varphi\varphi}^{(1)}\phi_{x,\varphi} + R(N_{x\varphi}^{(0)} + N_{x\varphi}^{(0)}u_{0,x} + N_{x\varphi}^{(1)}\phi_{x,x} + Q_{\varphi z}^{(0)}\phi_x)],$$

$$\mu_3 = \frac{1}{2R^2}[2N_{\varphi\varphi}^{(1)}\phi_\varphi - 2N_{\varphi\varphi}^{(0)}(w_{0,\varphi} - v_0) - RN_{x\varphi}^{(0)}w_{0,x}],$$

$$\mu_4 = N_{xx}^{(0)}v_{0,x} + N_{xx}^{(1)}\phi_{\varphi,x} + \frac{N_{x\varphi}^{(0)}}{2} + \frac{Q_{xz}^{(0)}}{2}\phi_\varphi + \frac{1}{2R}[N_{x\varphi}^{(0)}(v_{0,\varphi} + w_0) + N_{x\varphi}^{(1)}\phi_{\varphi,\varphi}],$$

$$\mu_5 = \frac{N_{\varphi\varphi}^{(0)}}{R} + \frac{N_{\varphi\varphi}^{(0)}}{R^2}(v_{0,\varphi} + w_0) + \frac{N_{\varphi\varphi}^{(1)}}{R^2}\phi_{\varphi,\varphi} + \frac{N_{x\varphi}^{(0)}}{2R}v_{0,x} + \frac{N_{x\varphi}^{(1)}}{2R}\phi_{\varphi,x} + \frac{Q_{\varphi z}^{(0)}}{2R}\phi_\varphi,$$

$$\mu_6 = \frac{N_{\varphi\varphi}^{(0)}}{R} + \frac{N_{\varphi\varphi}^{(0)}}{R^2}(v_{0,\varphi} + w_0) + \frac{N_{\varphi\varphi}^{(1)}}{R^2}\phi_{\varphi,\varphi} + \frac{N_{x\varphi}^{(0)}}{2R}v_{0,x} + \frac{N_{x\varphi}^{(1)}}{2R}\phi_{\varphi,x} + \frac{Q_{\varphi z}^{(0)}}{2R}\phi_\varphi,$$

$$\mu_7 = N_{xx}^{(0)}w_{0,x} + \frac{N_{x\varphi}^{(0)}}{2R}(w_{0,\varphi} - v_0) - \frac{N_{x\varphi}^{(1)}}{2R}\phi_\varphi + \frac{Q_{xz}^{(0)}}{2},$$

$$\mu_8 = \frac{N_{\varphi\varphi}^{(0)}}{R^2}(w_{0,\varphi} - v_0) - \frac{N_{\varphi\varphi}^{(1)}}{R^2}\phi_\varphi + \frac{N_{x\varphi}^{(0)}}{2R}w_{0,x} + \frac{Q_{\varphi z}^{(0)}}{2R},$$

$$\mu_9 = \frac{Q_{xz}^{(0)}}{2} + \frac{Q_{xz}^{(0)}}{2}u_{0,x} + \frac{Q_{xz}^{(1)}}{2}\phi_{x,x} + \frac{Q_{\varphi z}^{(0)}}{2R}u_{0,\varphi} + \frac{Q_{\varphi z}^{(1)}}{2R}\phi_{x,\varphi},$$

$$\mu_{10} = N_{xx}^{(1)} + N_{xx}^{(1)}u_{0,x} + \frac{N_{x\varphi}^{(1)}}{2R}u_{0,\varphi} + \frac{Q_{xz}^{(1)}}{2}\phi_x,$$

$$\mu_{11} = \frac{N_{\varphi\varphi}^{(1)}}{R^2}u_{0,\varphi} + \frac{N_{x\varphi}^{(1)}}{2R} + \frac{N_{x\varphi}^{(1)}}{2R}u_{0,x} + \frac{Q_{\varphi z}^{(1)}}{2R}\phi_x,$$

$$\mu_{12} = -\frac{N_{\varphi\varphi}^{(1)}}{R^2}(w_{0,\varphi} - v_0) - \frac{N_{x\varphi}^{(1)}}{2R}w_{0,x} + \frac{Q_{xz}^{(0)}}{2}v_{0,x} + \frac{Q_{xz}^{(1)}}{2}\phi_{\varphi,x}$$

$$+ \frac{Q_{\varphi z}^{(0)}}{2} + \frac{Q_{\varphi z}^{(0)}}{2R}(v_{0,\varphi} + w_0) + \frac{Q_{\varphi z}^{(1)}}{2R}\phi_{\varphi,\varphi},$$

$$\mu_{13} = N_{xx}^{(1)}v_{0,x} + \frac{N_{x\varphi}^{(1)}}{2} + \frac{N_{x\varphi}^{(1)}}{2R}(w_0 + v_{0,\varphi}) + \frac{Q_{xz}^{(1)}}{2}\phi_\varphi,$$

$$\mu_{14} = \frac{N_{\varphi\varphi}^{(1)}}{R} + \frac{N_{\varphi\varphi}^{(1)}}{R^2}(v_{0,\varphi} + w_0) + \frac{N_{x\varphi}^{(1)}}{2R}v_{0,x} + \frac{Q_{\varphi z}^{(1)}}{2R}\phi_\varphi.$$

Appendix B

An empirical model shown in Appendix A illustrates the Tsai–Pagano model [47, 48], which makes a combination of the expected longitudinal to the transversal term in the ratios of $3/8$ and $5/8$ to predict the Young modulus of polymer composite containing randomly oriented kenaf or jute fibres, respectively,

$$E = \frac{3}{8}E_1 + \frac{5}{8}E_2,$$

where E_1 and E_2 are the longitudinal and transversal elastic moduli calculated by the Halpin–Tsai model.
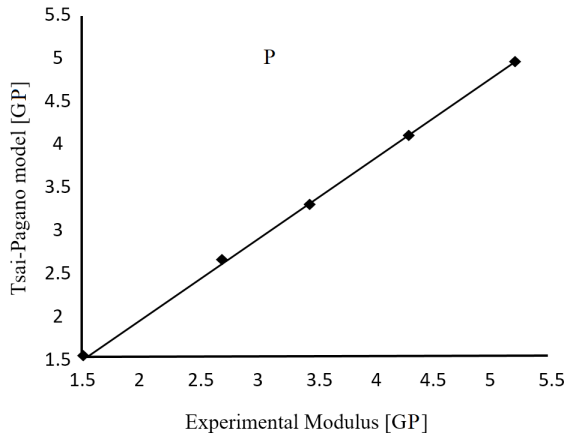

Fig. 9. Tsai–Pagano elastic modulus versus experimental Young's modulus for Polymer composite at each volume fraction [49].

A comparison of the Tsai–Pagano modeled elastic modulus with the experimental Young's modulus is presented in Fig. 9. The graph shows a good correlation of the Tsai–Pagano model with the experimental results.

Conflict of interest

The authors declare no conflict of interest.

References

1. G.N. Praveen, J.N. Reddy, *Nonlinear transient thermoelastic analysis of functionally graded ceramic-metal plates*, International Journal of Solids and Structures, **35**, 33, 4457–4476, 1998.

2. Y.Q. Wang, J.W. Zu, *Vibration behaviors of functionally graded rectangular plates with porosities and moving in thermal environment*, Aerospace Science and Technology, **69**, 550–562, 2017.

3. H. Kim, A.A. Abdala, C.W. Macosko, *Graphene/polymer nanocomposites*, Macromolecules, **43**, 16, 6515–6530, 2010.

4. A.M. Esawi, M.M. Farag, *Carbon nanotube reinforced composites: potential and current challenges*, Materials & Design, **28**, 9, 2394–2401, 2007.

5. K.M. Liew, Z.X. Lei, L.W. Zhang, *Mechanical analysis of functionally graded carbon nanotube reinforced composites: a review*, Composite Structures, **120**, 90–97, 2015.

6. R. Gholami, R. Ansari, *Large deflection geometrically nonlinear analysis of functionally graded multilayer graphene platelet-reinforced polymer composite rectangular plates*, Composite Structures, **180**, 760–771, 2017.

7. M.A. Rafiee, J. Rafiee, Z. Wang, H. Song, Z.Z. Yu, N. Koratkar, *Enhanced mechanical properties of nanocomposites at low graphene content*, ACS Nano, **3**, 12, 3884–3890, 2009.

8. C.H. Thai, A.J.M. Ferreira, T.D.Tran, P. Phung-Van, *Free vibration, buckling and bending analyses of multilayer functionally graded graphene nanoplatelets reinforced composite plates using the NURBS formulation*, Composite Structures, **220**, 749–759, 2019.

9. J. Liu, U. Khan, J. Coleman, B. Fernandez, P. Rodriguez, S. Naher, D. Brabazon, *Graphene oxide and graphene nanosheet reinforced aluminium matrix composites: powder synthesis and prepared composite characteristics*, Materials & Design, **94**, 87–94, 2016.

10. F. Lin, Y. Xiang, H.S. Shen, *Temperature dependent mechanical properties of graphene reinforced polymer nanocomposites–a molecular dynamics simulation*, Composites Part B: Engineering, **111**, 261–269, 2017.

11. M. Heidarhaei, M. Shariati, H. Eipakchi, *Experimental and analytical investigations of the tensile behavior of graphene-reinforced polymer nanocomposites*, Mechanics of Advanced Materials and Structures, 1–10, 2018.

12. H.S. Shen, Y. Xiang, F. Lin, D. Hui, *Buckling and postbuckling of functionally graded graphene-reinforced composite laminated plates in thermal environments*, Composites Part B: Engineering, 119, 67–78, 2017.

13. H. Wu, S. Kitipornchai, J. Yang, *Thermal buckling and postbuckling of functionally graded graphene nanocomposite plates*, Materials & Design, **132**, 430–441, 2017.

14. R.M.R. Reddy, W. Karunasena, W. Lokuge, *Free vibration of functionally graded-GPL reinforced composite plates with different boundary conditions*, Aerospace Science and Technology, **78**, 147–156, 2018.

15. H. Guo, S. Cao, T. Yang, Y. Chen, *Vibration of laminated composite quadrilateral plates reinforced with graphene nanoplatelets using the element-free IMLS-Ritz method*, International Journal of Mechanical Sciences, **142**, 610–621, 2018.

16. H. Wu, J. Yang, S. Kitipornchai, *Dynamic instability of functionally graded multilayer graphene nanocomposite beams in thermal environment*, Composite Structures, **162**, 244–254, 2017.

17. C. Feng, S. Kitipornchai, J. Yang, *Nonlinear bending of polymer nanocomposite beams reinforced with non-uniformly distributed graphene platelets (GPLs)*, Composites Part B: Engineering, **110**, 132–140, 2017.

18. M. Song, S. Kitipornchai, J. Yang, *Free and forced vibrations of functionally graded polymer composite plates reinforced with graphene nanoplatelets*, Composite Structures, **159**, 579–588, 2017.

19. J. Yang, H. Wu, S. Kitipornchai, *Buckling and postbuckling of functionally graded multilayer graphene platelet-reinforced composite beams*, Composite Structures, **161**, 111–118, 2017.

20. S. Sahmani, M.M. Aghdam, *Nonlinear instability of axially loaded functionally graded multilayer graphene platelet-reinforced nanoshells based on nonlocal strain gradient elasticity theory*, International Journal of Mechanical Sciences, **131**, 95–106, 2017.

21. M. Song, J. Yang, S. Kitipornchai, W. Zhu, *Buckling and postbuckling of biaxially compressed functionally graded multilayer graphene nanoplatelet-reinforced polymer composite plates*, International Journal of Mechanical Sciences, **131**, 345–355, 2017.

22. R. Gholami, R. Ansari, *Nonlinear harmonically excited vibration of third-order shear deformable functionally graded graphene platelet-reinforced composite rectangular plates*, Engineering Structures, **156**, 197–209, 2018.

23. Z. Zhou, Y. Ni, Z. Tong, S. Zhu, J. Sun, X. Xu, *Accurate nonlinear buckling analysis of functionally graded porous graphene platelet reinforced composite cylindrical shells*, International Journal of Mechanical Sciences, **151**, 537–550, 2019.

24. M. Arefi, E.M.R. Bidgoli, R. Dimitri, F. Tornabene, *Free vibrations of functionally graded polymer composite nanoplates reinforced with graphene nanoplatelets*, Aerospace Science and Technology, **81**, 108–117, 2018.

25. C.H. Thai, A.J.M. Ferreira, P. Phung-Van, *Size dependent free vibration analysis of multilayer functionally graded GPLRC microplates based on modified strain gradient theory*, Composites Part B: Engineering, **169**, 174–188, 2019.

26. P.H. Cong, N.D. Duc, *New approach to investigate the nonlinear dynamic response and vibration of a functionally graded multilayer graphene nanocomposite plate on a viscoelastic Pasternak medium in a thermal environment*, Acta Mechanica, **229**, 9, 3651–3670, 2018.

27. F. Bahranifard, M.R. Golbahar Haghighi, P. Malekzadeh, *In-plane responses of multilayer FG-GPLRC curved beams in thermal environment under moving load*, Acta Mechanica, **231**, 2679–2696, 2020.

28. A.W. Leissa, A.S. Kadi, *Curvature effects on shallow shell vibrations*, Journal of Sound and Vibration, **16**, 2, 173–187, 1971.

29. S.L. Lau, Y.K. Cheung, *Amplitude incremental variational principle for nonlinear vibration of elastic systems*, ASME Journal of Applied Mechanics, **48**, 959–964, 1981.

30. Y. Kobayashi, A. Leissa, *Large amplitude free vibration of thick shallow shells supported by shear diaphragms*, International Journal of Non-Linear Mechanics, **30**, 1, 57–66, 1995.

31. K.M. Liew, C.W. Lim, S. Kitipornchai, *Vibration of shallow shells: a review with bibliography*, Applied Mechanics Reviews, **50**, 431–444, 1997.

32. M. Amabili, M.P. Païdoussis, *Review of studies on geometrically nonlinear vibrations and dynamics of circular cylindrical shells and panels, with and without fluid-structure interaction*, Applied Mechanics Reviews, **56**, 4, 349–381, 2003.

33. T. Farsadi, M. Rahmanian, H. Kurtaran, *Nonlinear lay-up optimization of variable stiffness composite skew and taper cylindrical panels in free vibration*, Composite Structures, **262**, 113629, 2021.

34. H. Kurtaran, *Geometrically nonlinear transient analysis of thick deep composite curved beams with generalized differential quadrature method*, Composite Structures, **128**, 241–250, 2015.

35. T. Farsadi D. Asadi, H. Kurtaran, *Nonlinear flutter response of a composite plate applying curvilinear fiber paths*, Acta Mechanica, **231**, 2, 715–731, 2020.

36. T. Farsadi D. Asadi, H. Kurtaran, *Fundamental frequency optimization of variable stiffness composite skew plates*, Acta Mechanica, **232**, 2, 555–573, 2021.

37. T. Farsadi D. Asadi, H. Kurtaran, *Flutter improvement of a thin walled wing-engine system by applying curvilinear fiber path*, Aerospace Science and Technology, **93**, 2, 105353, 2019.

38. S. Abrate, M. Di Sciuva, *1.16 multilayer models for composite and sandwich structures*, Comprehensive Composite Materials II, **1**, 399–425, 2018.

39. M. Di Sciuva, *Bending, vibration and buckling of simply supported thick multilayered orthotropic plates: an evaluation of a new displacement model*, Journal of Sound and Vibration, **105**, 3, 425–442, 1986.

40. M. Di Sciuva, *An improved shear-deformation theory for moderately thick multilayered anisotropic shells and plates*, Journal of Applied Mechanics, **54**, 3, 589–596, 1987.

41. H. Darban, R. Massabò, *A homogenized structural model for shear deformable composites with compliant interlayers*, Multiscale and Multidisciplinary Modeling, Experiments and Design, **1**, 4, 269–290, 2018.

42. W. Han, M. Petyt, *Geometrically nonlinear vibration analysis of thin, rectangular plates using the hierarchical finite element method—I: the fundamental mode of isotropic plates*, Computers & Structures, **63**, 2, 295–308, 1997.

43. M. Song, S. Kitipornchai, J. Yang, *Free and forced vibrations of functionally graded polymer composite plates reinforced with graphene nanoplatelets*, Composite Structures, **159**, 579–588, 2017.

44. R. Benamar, *Nonlinear Dynamic Behaviour of Fully Clamped Beams and Rectangular Isotropic and Laminated Plates*, Doctoral Dissertation, University of Southampton, Southampton, 1990.

45. P. Ribeiro, *Non-linear free periodic vibrations of open cylindrical shallow shells*, Journal of Sound and Vibration, **313**, 1-2, 224–245, 2008.

46. V.N. Van Do, C.H. Lee, *Bézier extraction based isogeometric analysis for bending and free vibration behavior of multilayered functionally graded composite cylindrical panels reinforced with graphene platelets*, International Journal of Mechanical Sciences, **183**, 105744, 2020.

47. S.W. Tsai, J.C. Halpin, N.J. Pagano, *Invariant Properties of Composite Materials,* Composite Materials Workshop, Technomic Publication Corporation, Stamford, 1968.

48. J.C. Halpin, N.J. Pagano, *The laminate approximation for randomly oriented fibrous composites*, Journal of Composite Materials, **3**, 4, 720–724, 1969.

49. B.H. Lee, H.J. Kim, W.R. Yu, *Fabrication of long and discontinuous natural fiber reinforced polypropylene biocomposites and their mechanical properties*, Fibers and Polymers, **10**, 1, 83–90, 2009.